

# Self-Consistent Field Model Simulations for Statistics of Amorphous Polymer Chains in Crystalline Lamellar Structures

Takashi Uneyama<sup>1\*</sup>, Takafumi Miyata<sup>2</sup>, and Koh-hei Nitta<sup>1</sup>

<sup>1</sup> Institute of Science and Engineering, Kanazawa University,  
Kakuma, Kanazawa 920-1192, Japan

<sup>2</sup> Graduate School of Engineering, Nagoya University,  
Chikusa, Nagoya 464-8603, Japan

## Abstract

We calculate statistical properties of amorphous polymer chains between crystalline lamellae by self-consistent field model simulations. In our model, an amorphous subchain is modelled as a polymer chain of which ends are grafted onto the crystal-amorphous interfaces. The crystal-amorphous interfaces are expressed as impenetrable surfaces. We incorporate the interaction between segments to satisfy the incompressible condition for the segment density field. The simulation results show that amorphous polymer chains feel thin potential layers, which are mainly repulsive, near the crystal-amorphous interfaces. The impenetrable and incompressible conditions affect the statistics of polymer chains and the chain statistics becomes qualitatively different from the ideal Gaussian chain statistics without any constraints. We show the effects of the system size and the graft density to statistical quantities. We also show that the tie subchain statistics obey rather simple statistics.

## 1 Introduction

Crystalline polymers form various superstructures such as the crystalline lamellar structure, which consists of crystal and amorphous layers, and the spherulite structure[1, 2, 3, 4]. The mechanical properties of crystalline polymers depend on these superstructures. The crystalline lamellae strongly affect mechanical properties, and the relation between the crystalline lamellar structure and mechanical properties have been studied extensively[2, 3]. Especially, the statistics of tie subchains and tie molecules in crystalline lamellae is reported to be important for the mechanical properties[5, 6, 7, 8, 9, 10, 11]. Although considerable studies have been made for the statistics of tie subchains and tie molecules, it is not yet fully understood. Various theoretical models have been proposed for loop and tie subchains, and for tie molecules[12, 13, 14, 15, 16, 17, 18, 19]. For example, so-called the gambler’s ruin model[14] gives the statistics of amorphous subchains between crystalline lamellae. The Huang-Brown model[19] gives the estimate for the tie molecule fraction based on the ideal Gaussian chain statistics in melt before the crystallization. In what follows, we may call the Gaussian chain statistics in absence of inhomogeneous external fields as “the ideal Gaussian chain statistics.”

Simulations have been also utilized to study the statistics of tie subchains and tie molecules[20, 21, 22, 23, 24]. For example, we can compute various statistical quantities for tie subchains by the lattice Monte Carlo simulations and validate theoretical predictions. Due to the limitation of the computational resources, in most cases we need to employ coarse-grained models rather than atomistic models. These coarse-grained models involve some approximations and simplifications,

---

\*E-mail: uneyama@se.kanazawa-u.ac.jp, Tel: +81-76-264-6221, Fax: +81-76-234-4829

not all of which are justified. To simplify the model, in some cases (especially for off-lattice systems), the ideal Gaussian chain statistics is assumed without justification. However, the polymer chains in the amorphous phase interact each other rather strongly. The ideal Gaussian chain statistics is reproduced as a result of the screening effect[25], and naively, we expect that such a screening can be realized only in a bulk system. If the screening is not perfect, or if an external field is applied, the statistics of a polymer chain deviates from the ideal Gaussian chain statistics. In such cases, we need to take into account the contribution of the effective potential field.

In microphase separation structures of block copolymer melts, statistics of polymer chains are known to be qualitatively different from one of the bulk systems. For example, a diblock copolymer chain in a strongly segregated lamellar microphase separation structure is highly stretched, and the chain size (which is comparable to the lamellar period) scales as  $N^{2/3}$  (with  $N$  being the polymerization index)[26, 27, 28]. This is qualitatively different from the  $N$ -dependence of an ideal Gaussian chain size in a bulk,  $N^{1/2}$ . Polymer chains in the melt brush (dry brush) systems do not behave as ideal Gaussian chains, neither[29, 27, 28]. A polymer chain in a melt brush feels an inhomogeneous effective potential (pressure) field, and the free chain ends segregate into the surface of the brush. In both cases, the interaction between segments (or the incompressible condition for the segment density field) plays an important role. This implies that the interaction between segments can be also important in the crystalline lamellar systems.

Recently, Milner[30] investigated the nucleation process of polyethylene by simulations. To estimate the free energy barrier for the nucleation, he calculated the interfacial free energy between the bulk amorphous and the nucleus. The interface between the amorphous and the nucleus was modelled as the interface between infinitely large amorphous and crystal phases. Milner introduced the mean field potential field which makes the segment density spatially homogeneous (to satisfy the incompressible condition), and performed the lattice self-consistent field (SCF) simulations[27, 28, 31]. The simulation results showed the existence of a thin repulsive layer near the interface. Interestingly, the contributions of the mean field potential is not large except this repulsive layer. Although the repulsive layer is thin (just one lattice layer in the lattice SCF model), it affects the statistics of the polymer chains in the amorphous region rather strongly.

We consider that the situation is similar for the amorphous layers between crystalline lamellae. Namely, we expect that repulsive layers exist near the crystal-amorphous interfaces, and the statistics of the polymer chains in the amorphous region is largely affected by these repulsive layers. In this work, we propose a SCF model for the polymer subchains in the amorphous region between crystalline lamellae. We perform SCF simulations and show that the repulsive potential layers exist near the crystal-amorphous interfaces. Based on the simulation results, we calculate some statistical quantities of the amorphous subchains and discuss the statistics of the tie subchain in detail.

## 2 Model

### 2.1 Self-Consistent Field Model

We illustrate the schematic images of the crystalline lamellar structure and an amorphous region between crystalline lamellae in Figure 1 (a) and (b). In this work, we model an amorphous subchain between the crystalline lamellae as a grafted chain[30]. Both ends of a subchain are grafted onto the crystal-amorphous interfaces. For simplicity, we assume that the polymer chains are sufficiently long and the effects of the chain ends are negligible. (In other words, we do not consider the cilia subchains.) The interaction between segments is expressed via the mean field potential, which is determined self-consistently. From the symmetry, the one-dimensional system is sufficient for our simulations. We express the positions of the crystal-amorphous interfaces as  $x = 0$  and  $x = L$ . ( $L$  represents the thickness of the amorphous layer. In the followings we call  $L$  as the system size.)

The crystalline lamellar structure is formed when the melt is cooled. As known well, the thermal history, such as the quenching and annealing conditions, strongly affects the crystalline structure and subchain statistics[1, 2, 3, 4]. In this work, we consider the systems after sufficiently long annealing, and assume that the subchains in the system are well equilibrated. Under such

an assumption, the subchains obey the (local) equilibrium statistics, and the standard SCF model can be reasonably utilized.

The application of the SCF model to systems with hard and impenetrable walls have been done in various works[32, 33, 25]. Following the standard SCF model, the statistics of amorphous subchains can be described by using the path integral field. (See Appendix A for the detailed derivation of the SCF model.) As we mentioned, the system can be considered as one-dimensional. Thus, from the symmetry, the path integral field does not depend on  $y$  nor  $z$ . We express the path integral field (and other fields) as a function of  $x$ . The path integral field  $q(x, s)$  obeys the Edwards equation

$$\frac{\partial q(x, s)}{\partial s} = \frac{b^2}{6} \frac{\partial^2 q(x, s)}{\partial x^2} - v(x)q(x, s) \quad (1)$$

where  $s$  is the segment index,  $b$  is the segment size, and  $v(x)$  is the mean field potential. The boundary and initial conditions for eq (1) are

$$q(0, s) = q(L, s) = 0, \quad (2)$$

$$q(x, 0) = b[\delta(x - \epsilon) + \delta(x - L + \epsilon)]. \quad (3)$$

Here  $\epsilon$  is a small positive constant, and we take the limit of  $\epsilon \rightarrow 0$  at the end of the calculation. Eq (2) is the absorbing boundary condition which represents the effect of impenetrable regions[32]. In eq (3), we have introduced the numerical factor  $b$  so that the path integral field  $q(x, s)$  becomes dimensionless. (This numerical factor does not affect any thermodynamic properties such as the density.)

The density field  $\rho(x)$  is calculated from the path integral field  $q(x, s)$  as

$$\rho(x) = \frac{\bar{\sigma}}{\mathcal{Q}} \sum_{n=1}^{\infty} e^{\mu n/k_B T} \int_0^n ds q(x, s)q(x, n-s) \quad (4)$$

where  $\bar{\sigma}$  is the graft density (or the injection density),  $\mathcal{Q}$  is the single chain partition function (normalized by the interfacial area), and  $\mu$  is the chemical potential for segments. (This chemical potential is required to control the total number of segment in the system. In our model,  $\mu$  works as the Lagrange multiplier, and is automatically and uniquely determined, as we show below.) The single chain partition function is defined as follows:

$$\mathcal{Q} = \sum_{n=1}^{\infty} e^{\mu n/k_B T} \int_0^L dx q(x, 0)q(x, n). \quad (5)$$

We determine the chemical potential  $\mu$  so that the spatial average of the density field becomes a given value  $\bar{\rho}$  as

$$\bar{\rho} = \frac{1}{L} \int_0^L dx \rho(x). \quad (6)$$

Finally, the mean field potential  $v(x)$  is determined from the density field  $\rho(x)$ . In this work, we employ the harmonic potential

$$v(x) = \frac{1}{k_B T \bar{\rho}^2 \kappa} [\rho(x) - \bar{\rho}] \quad (7)$$

where  $\kappa$  is the compressibility[27]. We assume that the segment density field is almost constant ( $\rho(x) \approx \bar{\rho}$ ) due to the incompressible condition, and thus  $\kappa$  should be sufficiently small. The equilibrium solution is given as the set of fields which satisfies eqs (1)-(7) self-consistently.

The free energy of the system can be calculated from the self-consistent set of fields. For the harmonic potential (eq (7)), the explicit expression of the free energy becomes simply as follows:

$$\frac{\mathcal{F}}{k_B T} = -\frac{1}{2k_B T \bar{\rho}^2 \kappa} \int_0^L dx [\rho(x) - \bar{\rho}]^2 - \bar{\sigma} \ln \frac{e\mathcal{Q}}{\bar{\sigma}} \quad (8)$$

The free energy per unit volume is useful to study the thermodynamic stability of the obtained structure. In our model, the free energy per unit volume is simply expressed as  $f \equiv \mathcal{F}/L$ . To obtain the thermodynamic equilibrium structures, we need to minimize the free energy per unit volume with respect to the system size. Such a procedure is essential for microphase separation structures of block copolymers. However, the crystalline lamellar structure is not true thermodynamic equilibrium structure and thus we expect that there is no optimal system size which minimizes the free energy per unit volume. Therefore, in this work we do not minimize the free energy per unit volume with respect to the system size.

## 2.2 Numerical Scheme

In this subsection, we describe the discretization method and numerical scheme for the SCF simulations. We use the dimensionless units for simulations, by setting  $b = 1$  and  $k_B T = 1$ . There are roughly two numerical methods to solve the SCF model. One is the Fourier spectral method[28] and another is the real space method[34, 31]. Generally, the Fourier spectral method is preferred if the symmetry of the system is known. This is because the Fourier spectral method gives accurate results with relatively small numerical costs. However, in our case, the Fourier spectral method does not work as usual, due to the singularity of the mean field potential field. (We will discuss this point later.) Thus we employ the real space method, and discretize  $q(x, s)$ ,  $\rho(x)$  and  $v(x)$  by using a one dimensional regular mesh. We divide the system into  $m$  mesh points, and express the position of the  $i$ -th mesh point as  $x_i = (i + 1/2)L/m$  ( $i = 0, 1, 2, \dots, m - 1$ ). For convenience, we express the mesh size as  $h \equiv L/m$ . Also, we express the discretized fields as  $q_i(s)$ ,  $\rho_i$ , and  $v_i$  in the followings.

We approximate the spatial derivative in eq (1) by the central difference scheme. Then eq (1) with the boundary condition (2) can be discretized as

$$\frac{dq_i(s)}{ds} = - \sum_j C_{ij} q_j(s) \quad (9)$$

with the coefficient matrix  $C_{ij}$  defined as

$$C_{ij} \equiv \begin{cases} 1/3h^2 + v_i & (i = j), \\ -1/6h^2 & (i = j \pm 1), \\ 0 & (\text{otherwise}). \end{cases} \quad (10)$$

The initial condition (3) can be discretized as follows:

$$q_i(0) = \frac{1}{h}(\delta_{i,0} + \delta_{i,m-1}). \quad (11)$$

We can solve eq (9), by using the eigenvalues and eigenvectors of  $C_{ij}$  (just like the Fourier spectral method [28]),

$$q_i(s) = \sum_j U_{ij} e^{-s\lambda_j} p_j \quad (12)$$

where  $\lambda_j$  and  $U_{ij}$  represent the  $j$ -th eigenvalue and eigenvector, respectively.  $p_i$  is defined as

$$p_i \equiv \sum_j U_{ji} q_j(0) = \frac{1}{h}(U_{0,i} + U_{m-1,i}). \quad (13)$$

We can rewrite the discretized versions of eqs (4)-(7) by using the eigenvalues and eigenvectors. Eqs (4) and (5) become

$$\rho_i = \frac{\bar{\sigma}}{\mathcal{Q}} G_i \quad (14)$$

and

$$\mathcal{Q} = h \sum_i \frac{e^{-\lambda_i + \mu}}{1 - e^{-\lambda_i + \mu}} p_i^2 \quad (15)$$

with  $G_i$  being defined as

$$G_i \equiv \sum_{j,k} U_{ij} U_{ik} \frac{1}{\lambda_k - \lambda_j} \left[ \frac{e^{-\lambda_j + \mu}}{1 - e^{-\lambda_j + \mu}} - \frac{e^{-\lambda_k + \mu}}{1 - e^{-\lambda_k + \mu}} \right] p_j p_k. \quad (16)$$

(In the case of  $j = k$  or degenerated eigenvalues, the factor  $1/(\lambda_k - \lambda_j)$  in eq (16) diverges. To avoid this divergence, for such cases we expand the expression in the summation into the series of  $\lambda_k - \lambda_j$ .) Eq (6) is discretized as

$$\bar{\rho} = \frac{h\bar{\sigma}}{QL} \sum_i \frac{e^{-\lambda_i + \mu}}{[1 - e^{-\lambda_i + \mu}]^2} p_i^2. \quad (17)$$

The chemical potential  $\mu$  in eqs (15) and (16) is numerically determined to satisfy eq (17). Eq (7) is simply discretized as

$$v_i = \frac{1}{\bar{\rho}^2 \kappa} (\rho_i - \bar{\rho}). \quad (18)$$

We perform simulations by solving eqs (9)-(18) numerically. We employ the iteration method, which is widely employed in the SCF simulations[27, 31]. The numerical scheme to solve the set of discretized equations is as follows.

1. Set an initial guess for the potential field  $v_i$  as  $v_i = 0$ .
2. Calculate the coefficient matrix  $C_{ij}$  (eq (10)) from  $v_i$  and calculate the eigenvalues and eigenvectors,  $\lambda_j$  and  $U_{ij}$ .
3. Calculate the chemical potential  $\mu$  by solving eq (17) numerically. (In this work we employ the bisection method.)
4. Calculate the density field  $\rho_i$  from the eigenvalues  $\lambda_j$ , eigenvectors  $U_{ij}$ , and chemical potential  $\mu$  by eqs (13)-(16).
5. Update the potential field  $v_i$  to  $v_i^{(\text{new})}$  as

$$v_i^{(\text{new})} = (1 - \theta)v_i + \frac{\theta}{\bar{\rho}^2 \kappa} (\rho_i - \bar{\rho}) \quad (19)$$

where  $\theta$  is a small positive constant (the update parameter).

6. Evaluate the residue  $R$  for  $v_i$ :

$$R \equiv \frac{1}{m} \sum_i \left| v_i - \frac{1}{\bar{\rho}^2 \kappa} (\rho_i - \bar{\rho}) \right|. \quad (20)$$

If the residue  $R$  is larger than a threshold value, then go to Step 2.

For the calculation of the eigenvalues and eigenvectors at Step 2, we utilize the DSTEV subroutine in LAPACK (the QR method) [35]. The eigenvalues and eigenvectors can be successfully calculated within an acceptable numerical error range. (We have also examined the DSTEMR subroutine, which utilizes the MRRR method[36], and have observed that the obtained eigenvalues and eigenvectors are almost the same as ones obtained by the DSTEV subroutine.) After the calculation converges, physical quantities can be calculated by using quantities such as  $\lambda_i$  and  $U_{ij}$ . For example, the fraction of the subchain which consists of  $n$  segments (the segment number distribution) is calculated as

$$\phi(n) = \frac{h}{Q} \sum_i e^{-n(\lambda_i - \mu)} p_i^2. \quad (21)$$

By discretizing eq (8), we have the following expression for the free energy per unit volume:

$$f = -\frac{1}{2\bar{\rho}^2 \kappa m} \sum_i (\rho_i - \bar{\rho})^2 - \frac{\bar{\sigma}}{L} \left( \ln \frac{Q}{\bar{\sigma}} + 1 \right). \quad (22)$$

The statistics of the tie and loop subchains can be calculated by changing the initial condition (the graft condition). For the calculation of the loop subchain of which ends are grafted to the interface at  $x = 0$ , we use the initial condition

$$q_i(0) = \frac{1}{h} \delta_{i,0} \quad (23)$$

instead of eq (11). The calculation with the initial condition eq (23) can be easily performed by replacing the vector  $p_i$  by the following vector:

$$\tilde{p}_i \equiv \frac{1}{h} U_{0,i}. \quad (24)$$

The (discretized) density field of the loop subchains of which ends are grafted to the interface at  $x = 0$  is

$$\rho_{l,i} = \frac{\bar{\sigma}}{\mathcal{Q}} \tilde{G}_i \quad (25)$$

where  $\tilde{G}_i$  is defined by eq (16) with  $G_i$  and  $p_i$  replaced by  $\tilde{G}_i$  and  $\tilde{p}_i$ , respectively. From the symmetry, the density field of the loop subchains of which ends are grafted to the interface at  $x = L$  is simply given as

$$\rho'_{l,i} = \rho_{l,m-1-i} \quad (26)$$

and the density field of tie subchains is calculated as

$$\rho_{t,i} = \rho_i - \rho_{l,i} - \rho'_{l,i}. \quad (27)$$

The segment number distributions for the tie and loop subchains are calculated in a similar way.

$$\phi_l(n) = \frac{2h}{\mathcal{Q}} \sum_i e^{-n(\lambda_i - \mu)} \tilde{p}_i^2, \quad (28)$$

$$\phi_t(n) = \phi(n) - \phi_l(n). \quad (29)$$

For convenience, in the followings, we call  $\phi_l(n)$  and  $\phi_t(n)$  as the tie and loop subchain distribution functions, respectively.

### 3 Results

We perform the SCF simulations with the numerical scheme shown in Section 2.2. We fix the average segment density as  $\bar{\rho} = 1$ , and vary the graft density  $\bar{\sigma}$  and the system size  $L$ . We also fix the mesh size as  $h = 1/8$  and thus the number of mesh points is  $m = 8L$ . The compressibility is empirically chosen to be  $\bar{\kappa} = 0.001$ . This value is sufficiently small to realize almost constant segment density fields and approximately satisfy the incompressible condition. The update parameter  $\theta$  is also empirically chosen to make the iterations stable. Although the optimal value of  $\theta$  depends on other parameters, the typical value is of the order of  $10^{-4}$ . We set the tolerance value for the iteration as  $10^{-7}$ . (The effects of these parameters are rather minor. If we perform simulations with the different values of  $\theta$  and the tolerance, the obtained results are almost the same as the original result.)

#### 3.1 Density and Potential Fields

Firstly, we show the profiles of the segment densities of subchains and the effective potential for segments. Figure 2 shows the segment density profiles for the tie, loop, and all subchains for  $L = 8$  and  $\bar{\sigma} = 1$ , as an example. The segment density of all subchains is almost constant, which means that the incompressible condition is approximately satisfied. The loop subchain density field is high near the crystal-amorphous interface and decrease as the distance from the interface increases. On

the other hand, the tie subchain density field is very low near the crystal-amorphous interface and is high near the center of the amorphous region. In other words, the tie subchain segments are concentrated in the center of the amorphous region.

Interestingly, the tie subchain density seems to be the same as the total loop subchain densities at the center of the system,  $\rho_t(L/2) = \rho_l(L/2) + \rho'_l(L/2)$ . This implies that the relation  $\rho_t(L/2) = \bar{\rho}/2$  holds. This can be intuitively understood from the symmetry argument, as follows. If we find a subchain of one of which segments is at the center of the amorphous region, the probabilities that one end of the subchain is connected to the crystal-amorphous interface at  $x = 0$  and  $x = L$  are the same. Thus we find the tie subchain and the loop subchain by the equal probabilities. Figure 3 shows the system size and graft density dependence of the tie segment density profile. We can observe that  $\rho_t(L/2) = \bar{\rho}/2$  actually holds for various values of  $L$  and  $\bar{\sigma}$ . The tie segment density profile near the interface strongly depends on  $L$  and  $\bar{\sigma}$ . The tie segment density near the interface decreases as  $L$  increases or as  $\bar{\sigma}$  increases.

Figure 4 shows the effective mean field potential profile for segments, for  $L = 8$  and  $\bar{\sigma} = 1$  (which are the same parameters as the simulation shown in Figure 2). We can observe that the potential field is almost constant except the narrow regions near the crystal-amorphous interfaces. This result is similar to the Milner's simulation results. However, unlike Milner's results, our result shows that the potential layers near the interfaces are not purely repulsive. The potential layer consists of a thin attractive part and a broad repulsive part. We will discuss this in detail, later. We show the system size and graft density dependence of the potential profiles in Figure 5. As shown in Figure 5(a), the potential profile near the interface is almost independent of the system size  $L$ . On the other hand, the graft density  $\bar{\sigma}$  affects the potential profile rather strongly. Thus we expect that the mean field potential is primarily controlled by the graft density. The potential barrier near the crystal-amorphous interfaces repel segments so that the segment density becomes spatially homogeneous. The required potential barrier to satisfy the incompressible condition increases as the graft density increases.

If the compressibility is not small, the density profile deviates from the homogeneous profile. We show the simulations for compressible systems in Appendix B. In the cases of relatively large  $\kappa$  values, the segment density near the crystal-amorphous interface increases and the segment density near the system center decreases. The strength of the potential layers decreases as the density profile deviates from the homogeneous one.

Before we analyze the tie and loop subchain statistics, here we briefly examine the thermodynamic stability of the obtained structures. The thermodynamic stability of the structure is determined by the free energy per unit volume. Figure 6 shows the dependence of the free energy per unit volume  $f$  to the system size  $L$  and to the graft density  $\bar{\sigma}$ . From Figure 6(a),  $f$  monotonically decreases as  $L$  increases. This means that our system has no thermodynamically optimal size, as expected. On the other hand, as observed in Figure 6(b),  $f$  is not a monotonic function of  $\bar{\sigma}$ . This means that there is the optimal graft density which is thermally stable. However, we should recall that the graft density is not freely tunable in our system, because it is determined by the structure of the crystalline phase.

### 3.2 Tie and Loop Distributions

Secondly, we show the tie and loop subchain distributions. Figure 7 shows the subchain distributions for tie, loop, and all subchains. The loop subchain distribution  $\phi_l(n)$  decreases rapidly as  $n$  increases. This means that most of loop subchains are short. If we consider the loop subchain with  $n = 1$  as the tight loop which forms the adjacent reentry[12], the fraction of the tight loop becomes 0.55. This value is not so different from the prediction of the gambler's ruin model[14],  $2/3$ . The average numbers of segments for all subchains,  $\bar{n}$ , can be calculated as

$$\bar{n} = \frac{\bar{\rho}L}{\bar{\sigma}}. \quad (30)$$

Thus we have  $\bar{n} = 8$  for the current system ( $L = 8$ ,  $\bar{\sigma} = 1$ , and  $\bar{\rho} = 1$ ). The tie subchain distribution shown in Figure 7 has a maximum at  $n = 33$ , which is much larger than  $\bar{n}$ . Thus most of the tie

subchains consist of larger number of segments than  $\bar{n}$ . For  $n \gtrsim 50$ , the tie and loop subchain distributions almost coincide. As we mentioned, the probabilities that a segment near the system center belongs to tie and loop subchains are expected to be almost the same. Thus it seems to be natural that the tie and loop subchains distributions almost coincide for large  $n$ .

We show the total tie and loop subchain fractions defined as

$$\bar{\phi}_l = \sum_{n=1}^{\infty} \phi_l(n), \quad \bar{\phi}_t = \sum_{n=1}^{\infty} \phi_t(n) \quad (31)$$

for  $\bar{\sigma} = 1$  in Figure 8(a). For large  $L$ , the total tie subchain fraction can be expressed by a simple power-law type relation  $\phi_t(n) \propto L^{-1.03}$ . We show the graft density dependence of the total tie and loop subchain fractions for  $L = 8$  in Figure 8(b). The  $\bar{\sigma}$ -dependence of  $\bar{\phi}_t$  can also be fitted well by a power-law. The fitting of the power-law to the simulation data gives  $\bar{\phi}_t \propto \bar{\sigma}^{-0.81}$ . The decrease of the total tie subchain fraction may be caused as a result of the increase of the total loop subchain fraction by tight loop subchains. As observed in Figure 3(b), the tie segment density near the interface largely decreases as the graft density increases. We expect that this corresponds the increase of tight loops, and consequently the total tie subchain fraction decreases.

The average numbers of segments for tie and loop subchains,  $\bar{n}_l$  and  $\bar{n}_t$ , can be calculated from the subchain distributions:

$$\bar{n}_l = \frac{1}{\bar{\phi}_l} \sum_{n=1}^{\infty} n\phi_l(n), \quad \bar{n}_t = \frac{1}{\bar{\phi}_t} \sum_{n=1}^{\infty} n\phi_t(n). \quad (32)$$

We show the system size dependence of the average numbers of segments for tie, loop and all subchains in Figure 9(a). The average numbers of segments for all subchains,  $\bar{n}$ , in Figure 9(a) is calculated by eq (30). We also show the graft density dependence of the average numbers of segments in Figure 9(b). For all the parameters examined above,  $\bar{n}_t$  is always larger than  $\bar{n}_l$  and  $\bar{n}$ . Although the total number fraction of the tie subchain  $\bar{\phi}_t$  is small, The tie subchains consist of large number of segments compared with loop subchains. We can observe that for large  $L$ ,  $\bar{n}_t$  depends on  $L$  as  $\bar{n}_t \propto L^{2.06}$ . This  $L$ -dependence is qualitatively different from ones of  $\bar{n}$  and  $\bar{n}_l$  ( $\bar{n}, \bar{n}_l \propto L^1$ ). The  $\bar{\sigma}$ -dependence of  $\bar{n}_l$  is rather simple,  $\bar{n}_l \propto \bar{\sigma}^{-1}$ . The  $\bar{\sigma}$ -dependence of  $\bar{n}_t$ ,  $\bar{n}_t \propto \bar{\sigma}^{-0.34}$  is again different from the cases of  $\bar{n}$  and  $\bar{n}_l$ .

## 4 Discussions

### 4.1 Effective Potential Field

As shown in Section 3.1, the effective mean field potential is almost constant except the narrow regions near the crystal-amorphous interfaces. A potential layer near an crystal-amorphous interface consists of two sublayers. The first sublayer is very thin and attractive, whereas the second sublayer is rather broad and repulsive. This result is apparently inconsistent with the Milner's simulation results[30]. In this subsection, we discuss the repulsive layer in detail.

The first sublayer is very thin and seems to be singular. Whether this sublayer is singular or not can be easily confirmed by performing simulations with different mesh sizes. Figure 10 shows the mean field potential profiles calculated with different mesh sizes ( $h = 1/32, 1/16, 1/8$  and  $1/4$ ) for  $L = 8$  and  $\bar{\sigma} = 1$ . The potential near the wall depends on  $h$  strongly, which corresponds to the singular behavior. To examine the properly of the singular layer, we show the mesh size dependence of the potential depth at the interface,  $v_{m/2} - v_0$ , in Figure 11. The potential depth dependence of the mesh size is roughly estimated as  $(v_{m/2} - v_0) \propto h^{-2}$ . This mesh size dependence is much stronger than one of the delta function ( $\propto h^{-1}$ ), and thus the singular potential layer cannot be interpreted as a delta function type singular potential. The interpretation of such singularity is not trivial. As a possible explanation, we consider the modulation of the boundary condition. Such a mesh size dependence can be realized if we phenomenologically introduce the non-absorbing

boundary condition[37],

$$\left. \frac{\partial q(x, s)}{\partial x} \right|_{x=0} = -kq(0, s), \quad \left. \frac{\partial q(x, s)}{\partial x} \right|_{x=L} = kq(L, s) \quad (33)$$

instead of the absorbing boundary condition (eq (2)). Here  $k$  is a constant which represents the strength of the microscopic potential near the interface. Generally, eq (33) reflects the effect of the microscopic potential on the walls. In our system, we do not have the microscopic potential on the interfaces and thus the origin of eq (33) is not clear. It may arise from the competition between two strong constraints; the initial condition (3) and the original boundary condition (2). (The initial condition tends to increase the density near the interface whereas the original boundary condition tends to reduce it.) If we discretize eq (33), we have the same mesh size dependence of the potential (as shown in Appendix C). The singular potential layer is smeared out if we use relatively large mesh size ( $h = 1/4$  in Figure 10). The lattice SCF model roughly corresponds to the case of  $h \approx 1$ , and thus we expect that the singular layer cannot be observed in the lattice SCF simulations. Also, the lattice in the Milner's model does not deform, which constrain the local and strong stretching of chains. We consider these are the reason why our and Milner's models give apparently inconsistent potential fields.

It would be worth mentioning here that such a boundary condition makes numerical calculations difficult. The numerical constant  $k$  in eq (33) should be determined self-consistently, just as the potential field. Namely, the boundary condition changes during the iterations. This makes the use of the Fourier spectral method[28] difficult. Besides, the update of the potential field can be large and unstable if the update parameter  $\theta$  is not small. This is why the values of  $\theta$  in our simulations are much smaller than the usual SCF simulations.

The second sublayer is rather broad and gradually decays as the distance from the interface increases. As shown in Figure 10, the profile of the second sublayer is almost independent of the mesh size, and thus is not singular. The profile of the second sublayer depends on  $\bar{\sigma}$  rather strongly, while it is almost independent of  $L$ . In the examined parameter range, the width of the second sublayer is of the order of the segment size  $b$  (which was taken to be unity in the simulations). This is consistent with Milner's results.

From these observations, we consider that the incompressible condition modulates the boundary condition and makes the repulsive potential layers at the crystal-amorphous interfaces. The importance of the boundary condition depends on the level of the description. At fine levels (such as our simulations), the non-absorbing boundary condition (or the singular potential layer) becomes important. On the other hand, at coarse levels (such as the lattice SCF simulations), the effect of the boundary condition (or the singular sublayer) becomes not important and we may express the effects of the incompressible condition only by thin repulsive potential layers. The subchain statistics may be modeled in a similar way to the adsorption of polymer chains onto surfaces[38, 39]. Actually, Milner[30] proposed to model a subchain as a sequence of the trains and free loops. A similar model with two potential layers may be constructed. In such a coarse-grained model, the potential layers affect the statistics of the trains and free loops.

We expect that the thickness of the repulsive potential layer is determined as a result of the competition between the incompressible and graft conditions. The strength of the graft effect may be characterized by the graft density  $\bar{\sigma}$ . We expect  $\bar{\rho}$  can be utilized to characterize this condition (although the treatment of the incompressible condition is not that simple). Then, as a rough estimate, we expect that the ratio of these two parameters  $\bar{\sigma}/\bar{\rho}$  (which has the dimension of the length) determines the thickness of the repulsive layer. This rough argument seems to be consistent with the results in Figure 5. (The thickness increases as  $\sigma$  increases, and is independent of  $L$ .)

The existence of the non-absorbing boundary condition and the repulsive potential layer (or the existence of the two potential layers) affects the statistics of subchains in the amorphous region. The statistics of chains deviates from the ideal Gaussian chain statistics without any potential fields. This means that the naive assumption of the ideal Gaussian chain statistics may lead qualitatively incorrect results for some statistical quantities. For example, our simulation results show that the chain statistics strongly depends on the graft density  $\bar{\sigma}$ . However, some tie chain models are based on the statistics which is independent of the graft density does not show such

graft density dependence. The Huang-Brown type model[19] assumes that the tie chain statistics is essentially determined by the Gaussian chain statistics in the melt state. In such models, the effect of the graft density is not taken into account (at least explicitly).

It is worth mentioning that the effective potential fields obtained by our simulations (and by Milner’s simulations) are qualitatively much different from the potential fields in polymer brush systems[29, 27, 28]. In the case of the melt brush, the density profile is the constant and one chain end is grafted onto the wall. This situation is similar to our system. However, the potential field in melt brush depends strongly on the distance from the wall. This behavior is qualitatively different from our result. This may be due to the difference in conditions for the number of segments in a (sub)chain. In our model, the number of segments in a subchain is not constant and subchains can adjust its length freely. (Due to this mechanism, the constraints by the graft and incompressibility may be very weak, except near the crystal-amorphous interfaces.) On the other hand, in a melt brush, the number of segments in a grafted chain is constant.

## 4.2 Statistics of Tie Subchain

The statistics of the tie subchains deviates from one expected from the ideal Gaussian chain statistics. This would be observed clearly if we compare our simulation results with the estimates based on the ideal Gaussian chain statistics without any constraints. As shown in Appendix D, the tie subchain fraction decays exponentially as  $L$  increases for large  $L$ . This  $L$ -dependence is qualitatively different from the SCF simulation result where the absorbing boundary condition and the incompressible condition are imposed. Namely, we underestimates the tie subchain fraction if we assume the ideal Gaussian chain statistics. Besides, without constraints, the average number of segments of a tie subchain depends  $L$  as  $\bar{n}_t \propto L^{1.5}$  (for large  $L$ ), which is again qualitatively different from the SCF simulation result. Thus, the statistics of ideal Gaussian chains without any constraints cannot explain the statistics of subchains between crystalline lamellae. The boundary condition and the interaction between segments are essential for the tie subchain statistics.

From the SCF simulation results, we expect that the tie subchain fraction and the average number of segments of a tie subchain depend on the system size as

$$\bar{\phi}_t \propto L^{-1}, \quad \bar{n}_t \propto L^2. \quad (34)$$

Interestingly, this system size dependence of  $\bar{n}_t$  is the same as one of an ideal Gaussian chain. Although a tie subchain does not behave as an ideal Gaussian chain, some properties of the tie subchain may be reasonably modelled with the ideal Gaussian chain statistics. It should be mentioned here that these results are consistent with the lattice-based gambler’s ruin model[14]. We consider that this is because the incompressible and impenetrable conditions are satisfied in the gambler’s ruin model. Although the gambler’s ruin model does not utilize the effective mean field potential field, the incompressible condition can control the conformation of subchains and thus the resulting statistics becomes similar to the SCF model. It would be worth mentioning that the SCF model presented in this work is continuum and thus it is free from the limitations and artifacts of lattice-based models. For example, our model can continuously change the parameters such as  $L$  and  $\bar{\sigma}$ .

From the result in Section 4.1 together with the simple system size relation (eq (34)), we expect that there may be a universality for the tie subchain statistics. If the tie chain distribution is universal, we may be able to construct a master curve for the tie chain distribution function. To examine whether such a master curve can be constructed or not, we rescale the number of segments  $n$  and the tie chain distribution function  $\phi_t$  by the average number of segments  $\bar{n}_t$  and the total tie chain fraction  $\bar{\phi}_t$ , respectively. Figure 12 shows the rescaled tie chain distribution functions for various different values of  $L$  and  $\bar{\sigma}$ . We can observe that all the rescaled tie chain distributions collapse into one master curve within an acceptable error. Thus we conclude that the tie chain distribution function is universal (at least in the examined parameter range). Moreover, the master curve can be reasonably fitted to the following empirical form:

$$\frac{\phi_t(n/\bar{n}_t)}{\bar{\phi}_t} \propto \left(\frac{\bar{n}_t}{n}\right)^2 \exp\left(-\alpha\frac{\bar{n}_t}{n} - \beta\frac{n}{\bar{n}_t}\right) \quad (35)$$

where  $\alpha$  and  $\beta$  are fitting parameters. The fitting with the SCF simulation data (shown in Figure 12) gives  $\alpha \approx 1.4$  and  $\beta \approx 0.9$ .

Here it would be fair to mention the limitations of our SCF model. Although our model gives interesting results on the statistics of loop and tie subchains, it should be noticed that our model is based on some assumptions. We should be careful whether the assumptions are reasonable for the target systems or not. For example, if the molecular weight is small, the effect of free ends (cilia) is not negligible. The annealing may not fully equilibrate the subchains due to the very slow relaxation by trapped entanglements (true entanglements).

The trapped entanglements would largely affect the chain statistics. As an example, we consider two loop subchains which are connected to different interfaces. If two loop subchains are entangled, there are constraint on the conformations of subchains. (Unentangled conformations are not allowed.) This constraint affects the path integral field and the partition function. Intuitively, we expect that the long subchains are easily entangled, and thus the constraint by trapped entanglements becomes important especially for short subchains. Unfortunately, as far as the authors know, it is quite difficult to take into account the trapped entanglements into the continuum field models such as the SCF model. The extension of the SCF model, or the combination of the SCF and molecular models [40, 41, 42] would be required to study the effect of trapped entanglements. Despite these limitations, we believe that our model can still provide non-trivial results, and can be utilized to study statistics and properties of amorphous subchains.

### 4.3 Possible Applications

Our simulation models can handle various parameters and is suitable to determine some statistical quantities of the tie subchains, as shown in Section 3. Here we discuss how our model and results can be used for applications. A simple but interesting application is the combination of our simulation model with other coarse-grained simulation models. The combined simulations will enable us to perform large scale simulations with small computational costs. The modelling and simulations for larger systems (which consist of multiple crystalline and amorphous layers) are left for future works.

The free energy per unit volume may be utilized to analyze the multiple crystalline and amorphous layers. As shown in Figure 6(a), the free energy per unit volume decreases as the thickness of the amorphous layer increases. Intuitively, this can be interpreted as a repulsive interaction between crystal-amorphous interfaces which stabilize the crystalline lamellar structure.

The simulation results obtained in this work can also be used as inputs for theoretical models. For example, we can use the tie subchain distribution to estimate the whole chain conformation in multiple crystalline and amorphous layers. Such calculation gives the tie molecule fraction in annealed and well-equilibrated systems. Because the tie subchain statistics has rather simple properties (such as eqs (34) and (35)), some statistical quantities may be simple. We expect that the resulting tie molecule statistics will be applied to various systems (as long as the chains are well-equilibrated), and the comparison of thus estimated tie molecule statistics with experimental data is an interesting future work.

If we use the effective potential field as a mean-field potential for molecular simulations, some dynamical properties of amorphous subchains can be studied. Although the potential layer is thin, it may modulate the dynamics of amorphous subchains. We naturally expect that the segments near the graft points will behave in a qualitatively different way from the segments apart from the graft points. Such a picture is consistent with the three-phase models for crystalline polymers[43, 44]. In the three-phase models, there is an intermediate layer between crystalline and amorphous layers. Our model will be useful to estimate the properties of the intermediate layers.

Another interesting application is the annealing dynamics. The dynamic SCF model[27, 31] allows us to simulate the relaxational dynamics. By combining our model with the dynamic SCF model, the simulations for the relaxation of subchain distributions will be possible. Such simulations will give the time evolution of the tie subchain distribution. If we start the simulation from a nonequilibrium subchain distribution, the rearrangement of subchains will be observed. NMR experiments[45, 46] showed that the polymer chains diffuse between the crystal and amorphous

regions during the annealing, and fraction of tight and semi-rigid amorphous chains changes by annealing processes. The comparison of the simulation data and the NMR data will be interesting.

## 5 Conclusions

We proposed the SCF model for the amorphous chain statistics between crystalline lamellae. We also proposed a numerical scheme for the SCF model and performed simulations with various different system sizes and graft densities. In our model, the amorphous-crystal interfaces are modelled as impenetrable surfaces, and a subchain is modelled as a graft chain. We explicitly took into account the incompressible condition, which originally arose from the interaction between segments. The SCF simulation results showed that there exist thin potential layers near the crystal-amorphous interfaces. A potential layer consists of two sublayers. The first sublayer is a singular attractive layer, which can be interpreted as the non-absorbing boundary condition. The second sublayer is a relatively broad repulsive layer. The statistics of subchains is affected by the potential layers.

The tie and loop subchain statistics were also calculated by the SCF simulations. The tie subchains consist of larger number of segments than the average. The system size dependence of the average number of segments in the tie subchain and tie subchain fraction obey rather simple statistics, and they are consistent with the prediction of the gambler's ruin model. We found that the tie subchain distribution function can be collapse into one master curve, if we rescale the tie subchain distribution and the segment number by the total tie subchain fraction and the average number of segments in a tie subchain, respectively.

## Acknowledgment

This work was supported by Grant-in-Aid (KAKENHI) for Young Scientists B 25800235. T. U. thanks Dr. Quan Chen (Penn State University) for informing him about Ref [32].

## Appendix

### A Derivation of the Self-Consistent Field Equations

Although the SCF model itself has been studied widely and its derivation for bulk systems is well known, the SCF model for grafted polymer systems with a variable segment number is not trivial. In this appendix, we show the detailed derivation of the SCF model in the main text. We start from a multichain system in a three dimensional box. We express the number of subchains of which segment number is  $n$  as  $M_n$ , and the conformation of the  $j$ -th subchain which consists of  $n$  segments as  $\mathbf{R}_{n,j}$ . From the nature of the crystalline structure, the segment number  $n$  should be discrete. For simplicity, we assume that  $n$  is an integer. The partition function  $\mathcal{Z}$  of the system is expressed as

$$\mathcal{Z} = \sum'_{\{M_n\}} \left[ \prod_{n=1}^{\infty} \frac{1}{M_n!} \right] \int \left[ \prod_{n=1}^{\infty} \prod_{j=1}^{M_n} \tilde{\mathcal{D}}\mathbf{R}_{n,j} \right] \exp \left[ -\frac{\mathcal{U}[\hat{\rho}]}{k_B T} + \frac{\mu}{k_B T} \sum_{n=1}^{\infty} n M_n \right]. \quad (36)$$

Here,  $\mu$  is the chemical potential for segments. The summation over  $\{M_n\}$  in (36) represents the summation under the constraint

$$\sum_{n=1}^{\infty} M_n = A\bar{\sigma}, \quad (37)$$

( $A$  is the interfacial area) and  $\int \tilde{\mathcal{D}}\mathbf{R}_{n,j}$  in eq (36) represents the functional integral over the conformation of an end-grafted subchain with the statistical weight of the ideal Gaussian chain:

$$\begin{aligned} \tilde{\mathcal{D}}\mathbf{R}_{n,j} &\equiv \mathcal{D}\mathbf{R}_{n,j} \exp \left[ - \int_0^n ds \frac{3}{2b^2} \left| \frac{\partial \mathbf{R}_{n,j}(s)}{\partial s} \right|^2 \right] \\ &\times b^2 [\delta(R_{n,j,x}(0) - \epsilon) + \delta(R_{n,j,x}(0) - L + \epsilon)] \\ &\times [\delta(R_{n,j,x}(n) - \epsilon) + \delta(R_{n,j,x}(n) - L + \epsilon)]. \end{aligned} \quad (38)$$

Because the amorphous chain cannot penetrate into the crystalline regions, the chain conformation should satisfy  $0 \leq R_{n,j,x}(s) \leq L$ . The functional integral over the conformation is calculated under this constraint. For simplicity, we assume that the measure for the functional integral is determined appropriately so that the functional integral becomes dimensionless.  $\hat{\rho}(\mathbf{r})$  is the microscopic segment density field defined as

$$\hat{\rho}(\mathbf{r}) \equiv \sum_{n=1}^{\infty} \sum_{j=1}^{M_n} \int_0^n ds \delta(\mathbf{r} - \mathbf{R}_{n,j}(s)), \quad (39)$$

and  $\mathcal{U}[\hat{\rho}]$  is the interaction potential between segments:

$$\mathcal{U}[\hat{\rho}] = \int d\mathbf{r} \frac{1}{2\kappa\bar{\rho}^2} [\hat{\rho}(\mathbf{r}) - \bar{\rho}]^2. \quad (40)$$

Here,  $\bar{\rho}$  and  $\kappa$  in eq (40) are the average segment density and the compressibility.

Following the standard procedure[31], we rewrite the partition function (36) in terms of the coarse-grained segment density field. Namely, we utilize the identity for the delta functional and introduce the coarse-grained density field  $\rho(\mathbf{r})$ ,

$$\begin{aligned} 1 &= \int \mathcal{D}\rho \delta[\rho - \hat{\rho}] \\ &= \int \mathcal{D}\rho \mathcal{D}w \exp \left[ i \int d\mathbf{r} w(\mathbf{r}) [\rho(\mathbf{r}) - \hat{\rho}(\mathbf{r})] \right] \end{aligned} \quad (41)$$

with  $w(\mathbf{r})$  being an auxiliary potential field. By inserting eq (41) into the right hand side of eq (36) and utilizing the Stirling's formula, we have

$$\mathcal{Z} = \sum'_{\{M_n\}} \int \mathcal{D}\rho \mathcal{D}w \exp \left[ - \frac{\mathcal{U}[\rho]}{k_B T} + i \int d\mathbf{r} w(\mathbf{r}) \rho(\mathbf{r}) + \sum_{n=1}^{\infty} M_n \ln \frac{e\mathcal{Q}(n)}{M_n} \right] \quad (42)$$

where  $\mathcal{Q}(n)$  is the partition function for a single subchain which consists of  $n$  segments:

$$\mathcal{Q}(n) \equiv e^{\mu n/k_B T} \int \tilde{\mathcal{D}}\mathbf{R}_n \exp \left[ - i \int_0^n ds w(\mathbf{R}_n(s)) \right]. \quad (43)$$

The approximate solution (the mean field solution) can be obtained by maximizing the integrand in the right hand side of eq (36) with respect to  $\{M_n\}$ ,  $\rho(\mathbf{r})$ , and  $w(\mathbf{r})$  (the saddle point approximation). We have the following set of equations as the saddle point condition:

$$0 = \ln \frac{\mathcal{Q}(n)}{M_n} + \nu, \quad (44)$$

$$0 = - \frac{1}{k_B T \kappa \bar{\rho}^2} [\rho(\mathbf{r}) - \bar{\rho}] + iw(\mathbf{r}), \quad (45)$$

$$0 = i\rho(\mathbf{r}) - i \sum_{n=1}^{\infty} \frac{M_n e^{\mu n/k_B T}}{\mathcal{Q}(n)} \int_0^n ds \int \tilde{\mathcal{D}}\mathbf{R}_n \delta(\mathbf{r} - \mathbf{R}_n(s)) \exp \left[ - i \int_0^n ds w(\mathbf{R}_n(s)) \right]. \quad (46)$$

Here we have introduced the Lagrange multiplier  $\nu$  for the constraint (37). (Physically, this Lagrange multiplier can be understood as the chemical potential for subchains.) From eqs (37) and (44), the Lagrange multiplier  $\nu$  is determined to be

$$\nu = \ln \frac{A\bar{\sigma}}{Q}. \quad (47)$$

where  $Q$  is the single chain partition function,

$$Q \equiv \sum_{n=1}^{\infty} Q(n). \quad (48)$$

Eqs (44) and (47) give the explicit expression for the subchain number  $M_n$ ,

$$M_n = \frac{A\bar{\sigma}Q(n)}{Q}. \quad (49)$$

For convenience, we define the mean field potential  $v(\mathbf{r})$  as

$$v(\mathbf{r}) \equiv iw(\mathbf{r}). \quad (50)$$

Because  $w(\mathbf{r})$  is pure imaginary at the saddle point,  $v(\mathbf{r})$  is real. By substituting eqs (49) and (50) into eqs (45) and (46), we have the modified saddle-point equations as

$$v(\mathbf{r}) = \frac{1}{k_B T \kappa \bar{\rho}^2} [\rho(\mathbf{r}) - \bar{\rho}], \quad (51)$$

$$\rho(\mathbf{r}) = \frac{A\bar{\sigma}}{Q} \sum_{n=1}^{\infty} e^{\mu n/k_B T} \int_0^n ds \int \tilde{D}\mathbf{R}_n \delta(\mathbf{r} - \mathbf{R}_n(s)) \exp \left[ - \int_0^n ds v(\mathbf{R}_n(s)) \right]. \quad (52)$$

The free energy of the system under the saddle point approximation becomes

$$\frac{\mathcal{F}}{k_B T} = \ln \mathcal{Z} \approx \frac{\mathcal{U}[\rho]}{k_B T} - \int d\mathbf{r} v(\mathbf{r}) \rho(\mathbf{r}) - A\bar{\sigma} \ln \frac{eQ}{A\bar{\sigma}}. \quad (53)$$

From the symmetry of the system,  $v(\mathbf{r})$  and  $\rho(\mathbf{r})$  do not depend on  $y$  nor  $z$ . This means that the system can be treated as one dimensional. Therefore it is sufficient for us to consider the physical quantities per unit interfacial area. This is equivalent to simply set  $A = 1$ . The one dimensional version of eq (51) is eq (7). The one dimensional version of eq (52) can be rewritten in terms of the path integral field and the partial differential equation, by using the Feynman-Kac formula[47]. The resulting equations are eqs (1)-(4). Similarly, eqs (43) and (48) gives eq (5). In addition, we impose the condition that the total number of segments in the system is constant, and regard the chemical potential  $\mu$  as the Lagrange multiplier for this condition. This gives eq (6) as the constraint. The one dimensional version of eq (53) with the harmonic potential is eq (8). Thus we have the SCF model in the main text (the set of eqs (1)-(8)).

## B Effect of Compressibility on Density and Potential Fields

In the SCF simulations in the main text, we empirically choose  $\kappa = 0.001$ . As we mentioned, this value of  $\kappa$  is sufficient to reproduce almost incompressible density profiles. In this appendix, we perform simulations with different  $\kappa$  values ( $\kappa = 10^{-4} \sim 10^1$ ) and discuss what happens if the system becomes compressible.

We show the total segment density field  $\rho(x)$  and the effective potential  $v(x)$  for various values of  $\kappa$  (and  $\bar{\sigma} = 1$  and  $L = 8$ ) in Figures 13 and 14. We can observe that if  $\kappa$  is sufficiently small ( $\kappa = 10^{-3}$  and  $10^{-4}$ ), both the density and potential profiles become almost  $\kappa$ -independent. Therefore, we consider the system is practically incompressible for  $\kappa \lesssim 10^{-3}$ . This justifies our empirical choice of  $\kappa = 10^{-3}$  in the main text.

As  $\kappa$  increases, the potential and density profiles deviate from those for the incompressible system. From Figure 13, we can observe that the density near the wall increases and the density near the system center decreases, as  $\kappa$  increases. From Figure 14, we can also observe the height of the repulsive potential layer decreases as  $\kappa$  increases. These results are consistent with our discussion in the main text. The potential layer near the wall repel the segments to make the density field constant. Conversely, for small  $\kappa$  cases, the potential layer does not work well and the segments become relatively concentrated near the wall. The reduction of the density near the system center can be directly related to the reduction of the tie subchains, because we have the relation  $\rho_t(L/2) = \rho(L/2)/2$  at the system center and the tie segments are concentrated near the system center. As a result, the fraction of the tie subchains decreases as  $\kappa$  increases.

## C Discretization of Non-Absorbing Boundary Condition

In this appendix, we show that the discretization of the non-absorbing gives singular potential (33) at the interface. Eq (33) can be discretized as

$$\frac{q_0 - q_{-1}}{h} = -k \frac{q_0 + q_{-1}}{2}, \quad \frac{q_m - q_{m-1}}{h} = k \frac{q_m + q_{m-1}}{2}. \quad (54)$$

Here  $q_0$  and  $q_m$  are virtual path integral fields at the lattice points at  $x_{-1} = -h/2$  and  $x_m = L+h/2$ , respectively. We can modify eq (54) as follows, to obtain the explicit expressions for  $q_{-1}$  and  $q_m$ .

$$q_{-1} = \frac{1 + kh/2}{1 - kh/2} q_0, \quad q_m = \frac{1 + kh/2}{1 - kh/2} q_{m-1}. \quad (55)$$

The second order derivatives of  $q(x)$  at  $x_0$  and  $x_{m-1}$  are then discretized as

$$\frac{q_{-1} - 2q_0 + q_1}{h^2} = \frac{q_{-1} - 2q_0}{h^2} + \frac{1 + kh/2}{h^2(1 - kh/2)} q_0, \quad (56)$$

$$\frac{q_{m-2} - 2q_{m-1} + q_m}{h^2} = \frac{q_{m-2} - 2q_{m-1}}{h^2} + \frac{1 + kh/2}{h^2(1 - kh/2)} q_m. \quad (57)$$

The first terms in the right hand sides of eqs (56) and (57) correspond to the discretized second order derivatives under the absorbing boundary condition (2). The coefficient matrix  $C_{ij}$  for the absorbing boundary condition is recovered if we replace  $v_0$  and  $v_{m-1}$  in eq (10) by

$$v_0^{(\text{eff})} = v_0 - \frac{1 + kh/2}{6h^2(1 - kh/2)}, \quad v_{m-1}^{(\text{eff})} = v_{m-1} - \frac{1 + kh/2}{6h^2(1 - kh/2)}. \quad (58)$$

(The potentials at other lattice points ( $v_1, v_2, \dots, v_{m-2}$ ) in eq (10) are not affected.)  $v_0^{(\text{eff})}$  and  $v_{m-1}^{(\text{eff})}$  can be interpreted as the effective potential field at the interface. If the mesh size is small, they depend on  $h$  as  $v_0^{(\text{eff})} \approx v_{m-1}^{(\text{eff})} \approx 1/6h^2$ . Thus we find that the non-absorbing boundary condition corresponds singular potential layers and the potential depth is proportional to  $h^{-2}$ .

## D Statistics of Tie Subchain without Constraints

In this appendix, we consider the systems without any constraint. Namely, we do not impose the incompressible constraint nor the absorbing boundary condition. The total tie subchain fraction can be estimated as follows. From the ideal Gaussian chain statistics, the probability to find a loop or tie subchain is the same as the probability to find the subchain of which end-to-end distance is 0 or  $L$ , respectively. Then, the tie and loop subchain distributions are approximately given as follows:

$$\phi_l(n) \approx \frac{1}{Z\sqrt{n}} e^{-\tilde{\mu}n}, \quad (59)$$

$$\phi_t(n) \approx \frac{1}{Z\sqrt{n}} e^{-\tilde{\mu}n - 3L^2/2nb^2}. \quad (60)$$

Here we have defined  $\tilde{\mu} \equiv -\mu/k_B T > 0$ , and  $\mathcal{Z}$  is the partition function:

$$\mathcal{Z} = \sum_{n=1}^{\infty} \frac{1}{\sqrt{n}} e^{-\tilde{\mu}n} (1 + e^{-3L^2/2nb^2}). \quad (61)$$

If  $L$  is not very small, the sum over  $n$  can be reasonably approximated by the integral over  $n$ . Then we have

$$\mathcal{Z} \approx \int_0^{\infty} dn \frac{1}{\sqrt{n}} e^{-\tilde{\mu}n} (1 + e^{-3L^2/2nb^2}) = \sqrt{\frac{\pi}{\tilde{\mu}}} (1 + e^{-\sqrt{6\tilde{\mu}L^2/b^2}}) \quad (62)$$

and the average number of segments  $\bar{n}$  is given as

$$\bar{n} = -\frac{\partial \ln \mathcal{Z}}{\partial \tilde{\mu}} \approx \frac{1}{2\tilde{\mu}} \left[ 1 + \frac{\sqrt{6\tilde{\mu}L^2/b^2}}{e^{\sqrt{6\tilde{\mu}L^2/b^2}} + 1} \right]. \quad (63)$$

Substituting eq (30) into eq (63) gives the relation between  $\tilde{\mu}$  and  $L$ :

$$\tilde{\mu} \approx \frac{\bar{\sigma}}{2\bar{\rho}L} \left[ 1 + \frac{\sqrt{6\tilde{\mu}L^2/b^2}}{e^{\sqrt{6\tilde{\mu}L^2/b^2}} + 1} \right]. \quad (64)$$

Although it is difficult to obtain the explicit expression of  $\tilde{\mu}$ , we find that the second term in the parenthesis in the right hand side of eq (64) becomes small both for small and large  $L$  cases. Thus we simply approximate  $\tilde{\mu}$  as  $\tilde{\mu} \approx \bar{\sigma}/2\bar{\rho}L$ . The total tie subchain fraction  $\bar{\phi}_t$  is calculated as

$$\bar{\phi}_t \approx \frac{1}{\mathcal{Z}} \int_0^{\infty} dn \frac{1}{\sqrt{n}} e^{-\tilde{\mu}n - 3L^2/2nb^2} \approx \frac{1}{e^{\sqrt{3\bar{\sigma}L/\bar{\rho}b^2}} + 1}. \quad (65)$$

The average number of segments of a tie subchain can be calculated in a similar way:

$$\bar{n}_t \approx \frac{1}{\bar{\phi}_t \mathcal{Z}} \int_0^{\infty} dn n \frac{1}{\sqrt{n}} e^{-\tilde{\mu}n - 3L^2/2nb^2} \approx \frac{\bar{\rho}L}{\bar{\sigma}} \left( 1 + \sqrt{\frac{3\bar{\sigma}L}{\bar{\rho}b^2}} \right). \quad (66)$$

If  $L$  is sufficiently large, eqs (65) and (66) can simply reduce to

$$\bar{\phi}_t \approx e^{-\sqrt{3\bar{\sigma}L/\bar{\rho}b^2}}, \quad \bar{n}_t \approx \sqrt{\frac{3\bar{\rho}L^3}{\bar{\sigma}b^2}}. \quad (67)$$

Therefore, for large  $L$ , the total tie subchain fraction decays exponentially as  $L^{1/2}$  increases. The average number of segments of a tie subchain depends on  $L$  as  $\bar{n}_t \propto L^{3/2}$ . As mentioned in the main text, these  $L$ -dependence is qualitatively different from the SCF simulation results.

## References

- [1] L. Mandelkern, *The crystalline state*, J. Mark, K. Ngai, W. Graessley, L. Mandelkern, E. Samulski, J. Koenig, and G. Wignall, eds. (Cambridge University Press, Cambridge, 2004), chap. 4, 3rd ed., in *Physical Properties of Polymers*.
- [2] G. Strobl, *The Physics of Polymers* (Springer, Berlin, 1997), 2nd ed.
- [3] R. Seguela, *J. Polym. Sci. B: Polym. Phys.* **43**, 1729 (2005).
- [4] R. J. Young and P. A. Lovell, *Introduction to Polymers* (Taylor and Francis, Boca Raton, 2011), 3rd ed.
- [5] W. R. Krigbaum, R.-J. Roe, and K. J. Smith Jr., *Polymer* **5**, 533 (1964).

- [6] J. H. Weiner and D. H. Berman, *Macromolecules* **17**, 2015 (1984).
- [7] R. H. Boyd, *Polymer* **26**, 1123 (1985).
- [8] X. Lu, R. Qian, and N. Brown, *Polymer* **36**, 4239 (1995).
- [9] M. Takayanagi and K. Nitta, *Macromol. Theory Simul.* **6**, 181 (1997).
- [10] K. Nitta and M. Takayanagi, *J. Polym. Sci. B: Polym. Phys.* **37**, 357 (1999).
- [11] K. Nitta and M. Takayanagi, *J. Macromol. Sci. B: Phys.* **42**, 107 (2003).
- [12] P. J. Flory, *J. Am. Soc. Chem.* **84**, 2857 (1962).
- [13] E. A. DiMarzio, C. M. Guttman, and J. D. Hoffman, *Polymer* **21**, 1379 (1980).
- [14] C. M. Guttman and E. A. DiMarzio, *Macromolecules* **15**, 525 (1982).
- [15] F. A. M. Leermakers, J. M. H. M. Scheutjens, and R. J. Gaylord, *Polymer* **25**, 1577 (1984).
- [16] P. J. Flory, D. Y. Yoon, and K. A. Dill, *Macromolecules* **17**, 862 (1984).
- [17] J. A. Marqusee and K. A. Dill, *Macromolecules* **19**, 2420 (1986).
- [18] L. Lin and A. S. Argon, *J. Material Sci.* **29**, 294 (1994).
- [19] Y.-L. Huang and N. Brown, *J. Polym. Sci.: Polym. Phys.* **29**, 129 (1999).
- [20] S. C. Mathur and W. L. Mattice, *Macromolecules* **20**, 2165 (1987).
- [21] M. L. Mansfield, *Polymer* **32**, 2883 (1990).
- [22] S. Balijepalli and G. C. Rutledge, *Macromol. Symp.* **133**, 71 (1998).
- [23] S. Balijepalli and G. C. Rutledge, *J. Chem. Phys.* **109**, 6523 (1998).
- [24] S. Balijepalli and G. C. Rutledge, *Comp. Theor. Polym. Sci.* **10**, 103 (2000).
- [25] P. G. de Gennes, *Scaling Concepts in Polymer Physics* (Cornell University Press, Ithaca, New York, 1979).
- [26] T. Ohta and K. Kawasaki, *Macromolecules* **19**, 2621 (1986).
- [27] T. Kawakatsu, *Statistical Physics of Polymers: An Introduction* (Springer Verlag, Berlin, 2004).
- [28] M. W. Matsen, *Self-Consistent Field Theory and Its Applications*, G. Gompper and M. Schick, eds. (Wiley, 2007), chap. 2, in *Soft Matter Vol. 1: Polymer Melts and Mixtures*.
- [29] S. T. Milner, T. A. Witten, and M. E. Cates, *Europhys. Lett.* **5**, 413 (1988).
- [30] S. T. Milner, *Soft Matter* **7**, 2909 (2011).
- [31] M. Müller and F. Schmid, *Adv. Polym. Sci.* **185**, 1 (2005).
- [32] E. A. DiMarzio, *J. Chem. Phys.* **42**, 2101 (1965).
- [33] A. K. Dolan and S. F. Edwards, *Proc. R. Soc. Lond. A* **337**, 509 (1974).
- [34] G. H. Fredrickson, V. Ganesan, and F. Drolet, *Macromolecules* **35**, 16 (2002).
- [35] E. Anderson, Z. Bai, C. Bischof, S. Blackford, J. Demmel, J. Dongarra, J. D. Croz, A. Greenbaum, S. Hammarling, A. McKenney, and D. Sorensen, *LAPACK Users' Guide* (SIAM, 1999), 3rd ed.

- [36] I. S. Dhillon, B. N. Perlett, and C. Vömel, *ACM Trans. Math. Software* **32**, 533 (2006).
- [37] P. G. de Gennes, *Rep. Prog. Phys.* **32**, 187 (1969).
- [38] P. G. de Gennes, *J. Phys. (Paris)* **37**, 1445 (1976).
- [39] A. N. Semenov, J. Bonet-Avalos, A. Johner, and J. F. Joanny, *Macromolecules* **29**, 2179 (1996).
- [40] A. F. Terzis, D. N. Theodorou, and A. Stroeks, *Macromolecules* **33**, 1385 (2000).
- [41] A. F. Terzis, D. N. Theodorou, and A. Stroeks, *Macromolecules* **33**, 1397 (2000).
- [42] K. C. Daoulas and M. Müller, *J. Chem. Phys.* **125**, 184904 (2006).
- [43] A. Sedighiamiri, T. B. van Erp, G. W. M. Peters, L. E. Govaert, and J. A. W. van Dommelen, *J. Polym. Sci. B: Polym. Phys.* **48**, 2173 (2010).
- [44] O. Gueguen, S. Ahzi, A. Makradi, and S. Belouettar, *Mech. Mater.* **42**, 1 (2010).
- [45] K. Schmidt-Rohr and H. W. Spiess, *Macromolecules* **24**, 5288 (1991).
- [46] C. Hedesiu, D. E. Demco, R. Kleppinger, A. A. Buda, B. Blümich, K. Remerie, and V. M. Litvinov, *Polymer* **48**, 763 (2007).
- [47] B. Øksendal, *Stochastic Differential Equations: An Introduction with Applications* (Springer, New York, 1998), 5th ed.

## Figure Captions

Figure 1: Schematic illustrations of (a) a crystalline lamellar structure and (b) an amorphous region in the crystalline lamellae. Grey and white colors represent crystal and amorphous regions, respectively, and solid curves represent polymer chains. A tie subchain connect two different crystalline lamellae whereas a loop subchain does not.

Figure 2: The segment densities of tie, loop, and all subchains, for  $L = 8$  and  $\bar{\sigma} = 1$ . Two dotted curves represent the segment densities of the loop subchain of which ends are grafted to  $x = 0$  or  $x = L$ .

Figure 3: The system size and graft density dependence of the tie segment density. (a) The system size dependence for  $\bar{\sigma} = 1$ , and (b) the graft density dependence for  $L = 8$ . The normalized position  $x/L$  is used.

Figure 4: The effective potential profile for segments for  $L = 8$  and  $\bar{\sigma} = 1$ . The potential is shifted so that the potential becomes zero at the system center,  $v(L/2) = 0$ .

Figure 5: The system size and graft density dependence of the effective potential profile. (a) The system size dependence for  $\bar{\sigma} = 1$ , and (b) the graft density dependence for  $L = 8$ . Only the profiles for  $x \leq L/2$  is shown.

Figure 6: The system size and graft density dependence of the free energy per unit volume. (a) The system size dependence for  $\bar{\sigma} = 1$  and (b) the graft density dependence for  $L = 8$ .

Figure 7: The subchain distributions for tie, loop, and all subchains. The system size and graft density are  $L = 8$  and  $\bar{\sigma} = 1$ .

Figure 8: The system size and graft density dependence of the total tie and loop subchain fractions. (a) The system size dependence for  $\bar{\sigma} = 1$ , and (b) the graft density dependence for  $L = 8$ . The dashed lines represent the power-law type relations  $\bar{\phi}_t \propto L^{-1.03}$  and  $\bar{\phi}_t \propto \bar{\sigma}^{-0.81}$ .

Figure 9: The system size and graft density dependence of the average number of segments for tie, loop, and all subchains. (a) The system size dependence for  $\bar{\sigma} = 1$ , and (b) the graft density dependence for  $L = 8$ . The dashed lines represent the power-law type relations  $\bar{n}_t \propto L^{2.06}$  and  $\bar{n}_t \propto \bar{\sigma}^{-0.34}$ .

Figure 10: The effective potential profile for  $L = 8$  and  $\bar{\sigma} = 1$ , calculated with various values of  $h$ . The strong  $h$ -dependence of the potential profile near  $x = 0$  implies the existence of a singular layer at  $x = 0$ .

Figure 11: The mesh size dependence of the potential depth at the crystal-amorphous interface,  $v_{m/2} - v_0$ . The dotted curve represents the power-law type relation  $v_{m/2} - v_0 \propto h^{-2}$ .

Figure 12: The rescaled tie subchain distribution functions for various  $L$  and  $\bar{\sigma}$ . The number of segments  $n$  and the tie chain distribution function  $\phi_t$  are rescaled by the average number of segment in a tie subchain  $\bar{n}_t$  and the total tie subchain fraction  $\bar{\phi}_t$ , respectively.

Figure 13: The compressibility dependence of the total density for  $\bar{\sigma} = 1$  and  $L = 8$ . Only the profiles for  $x \leq L/2$  is shown.

Figure 14: The compressibility dependence of the effective potential field for  $\bar{\sigma} = 1$  and  $L = 8$ . Only the profiles for  $x \leq L/2$  is shown.

# Figures

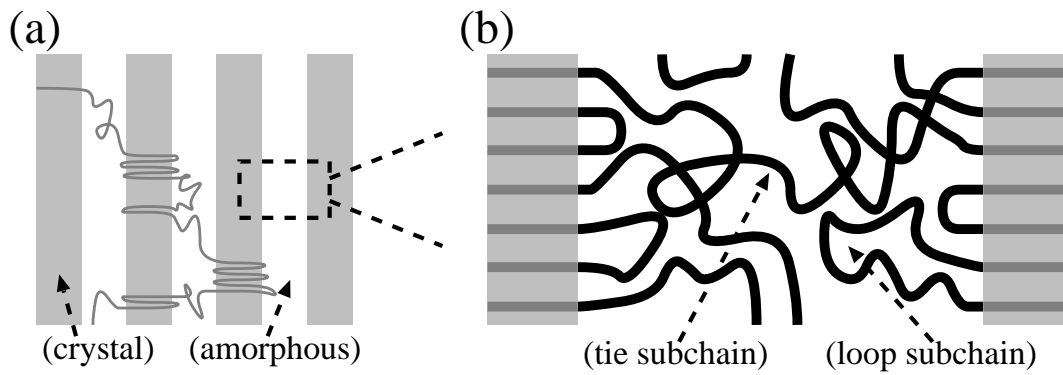


Figure 1:

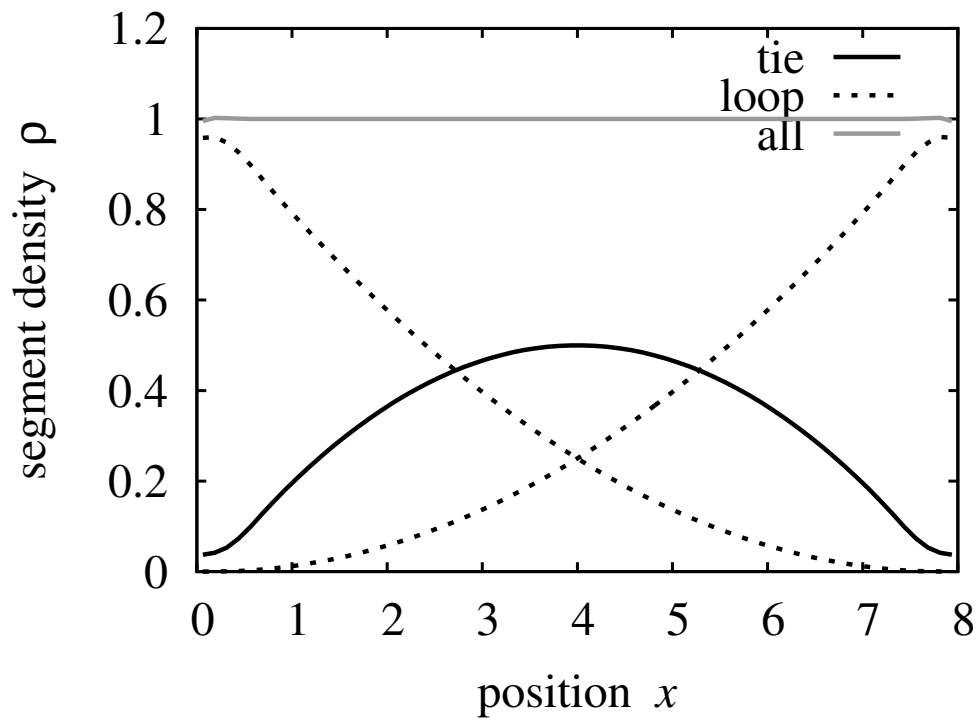


Figure 2:

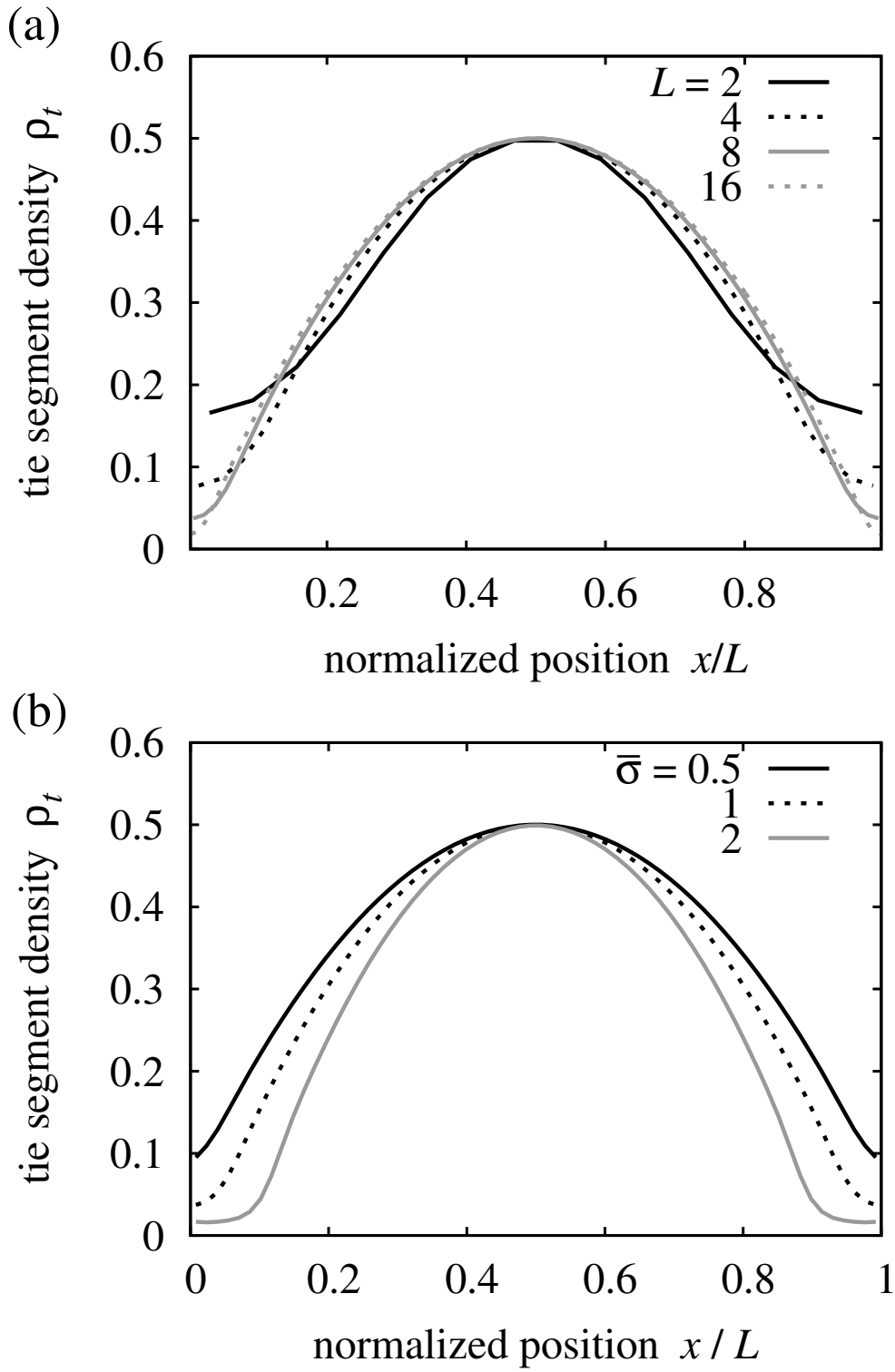


Figure 3:

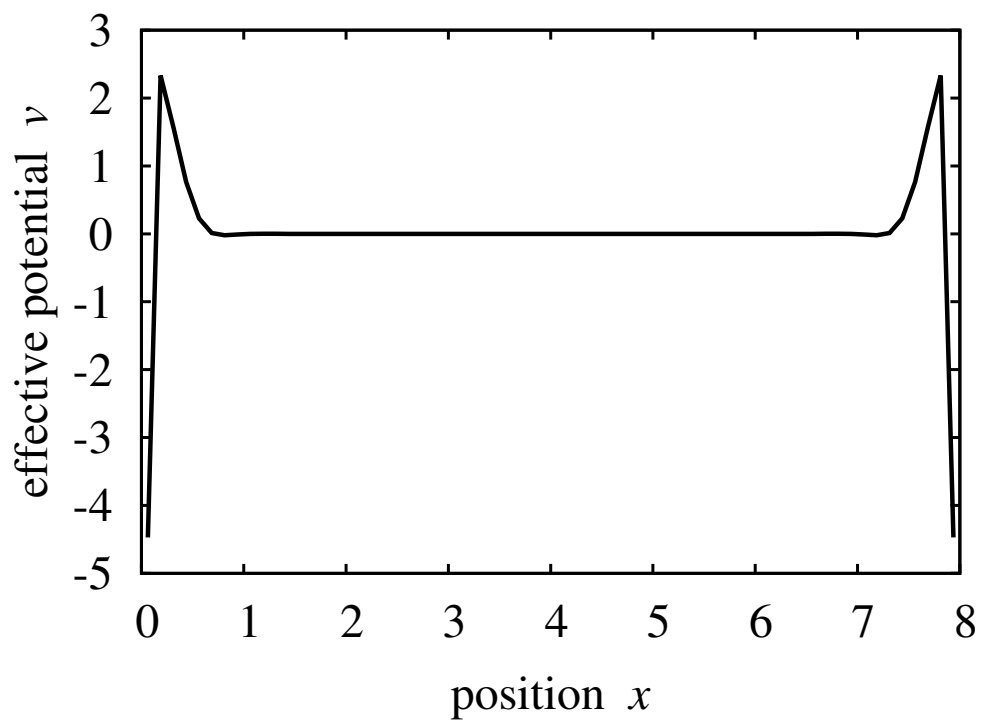


Figure 4:

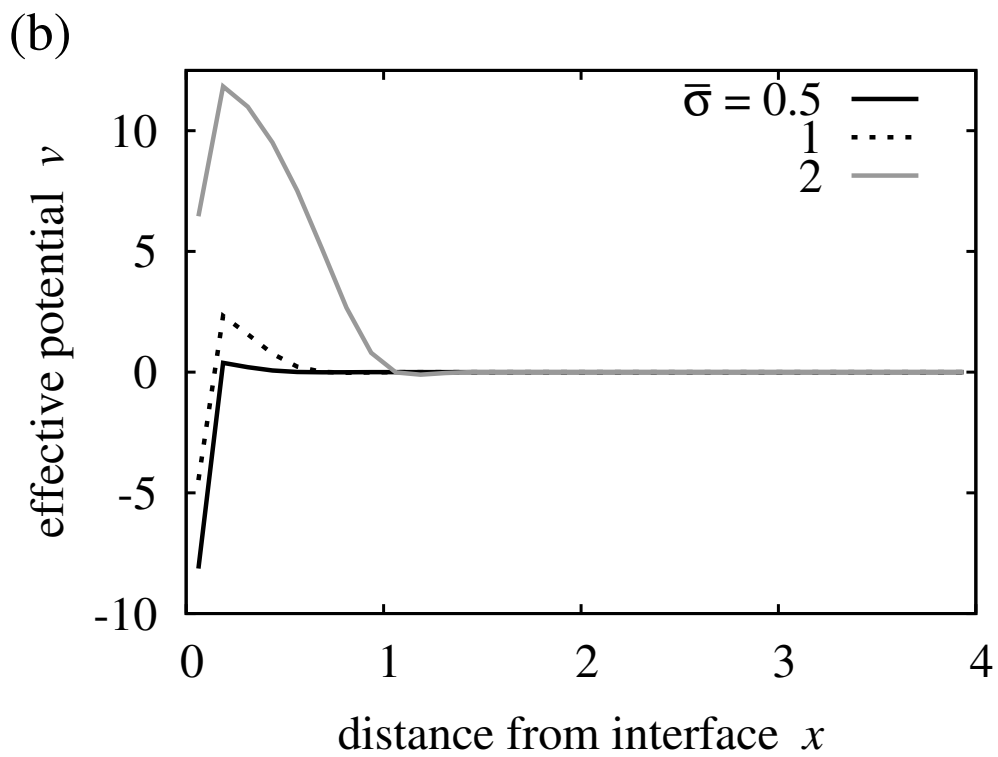
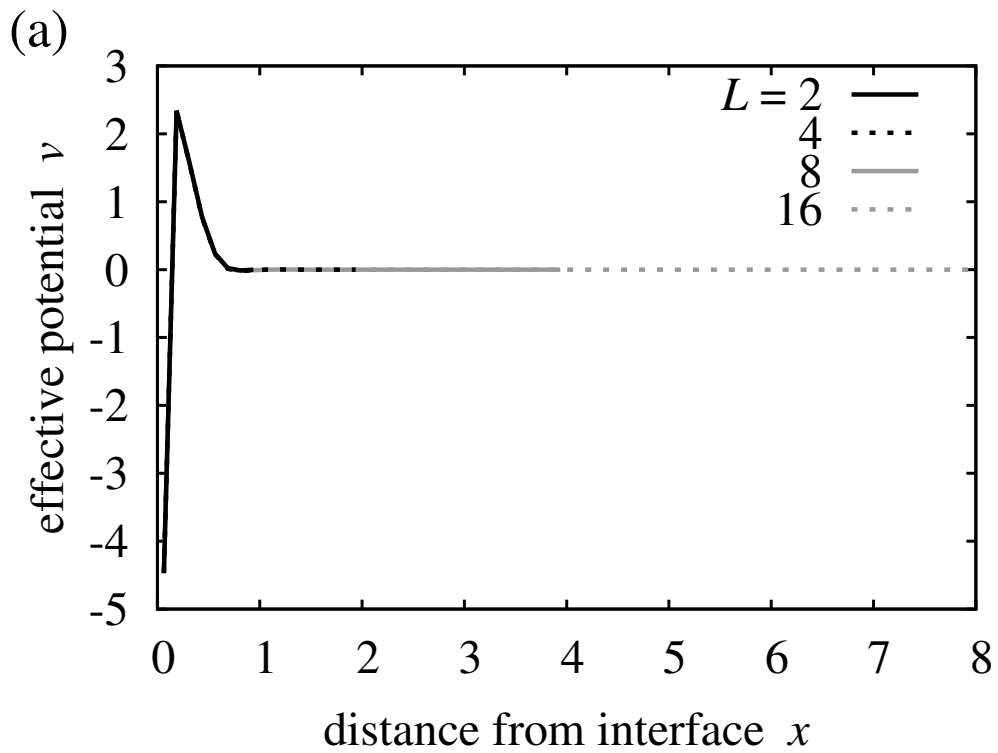


Figure 5:

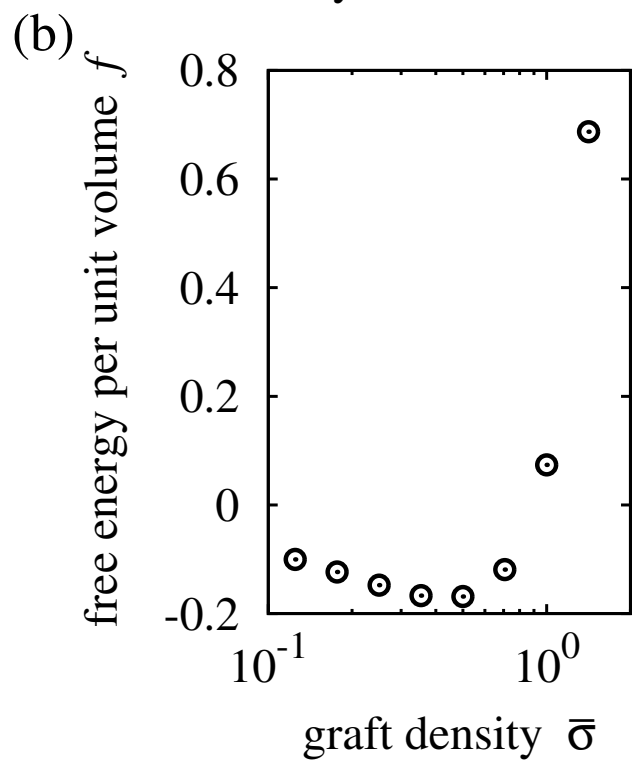
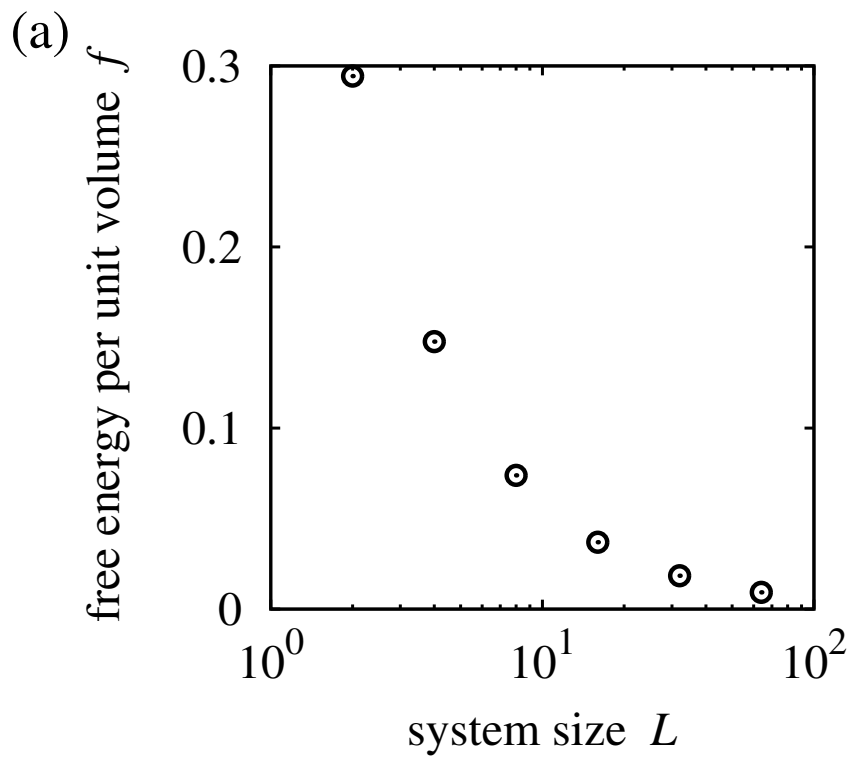


Figure 6:

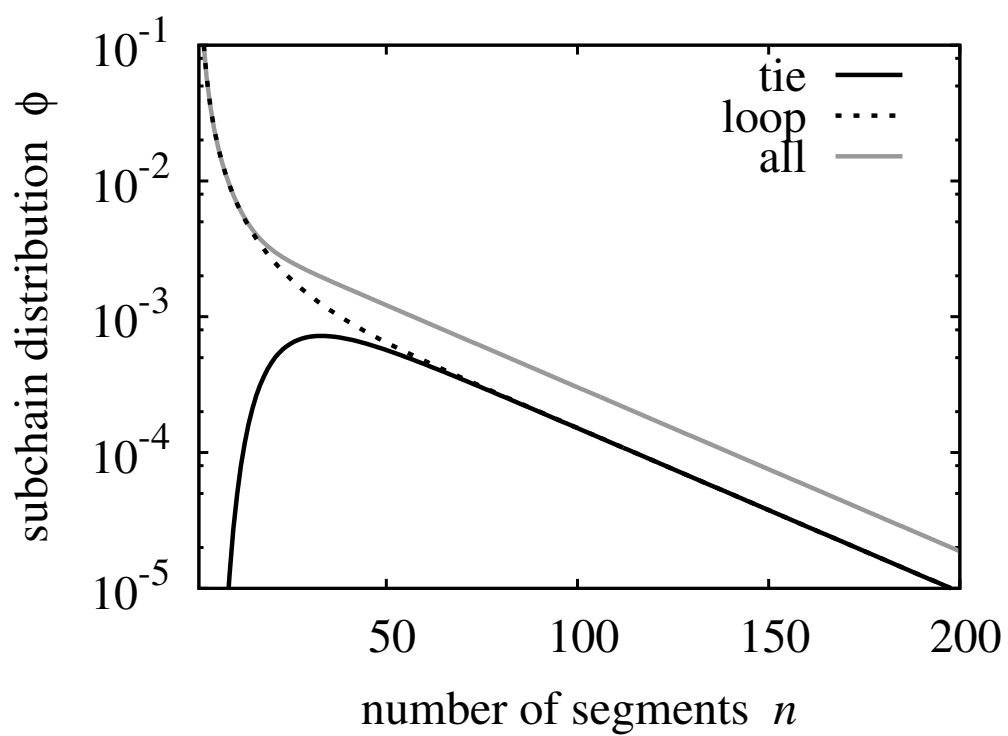


Figure 7:

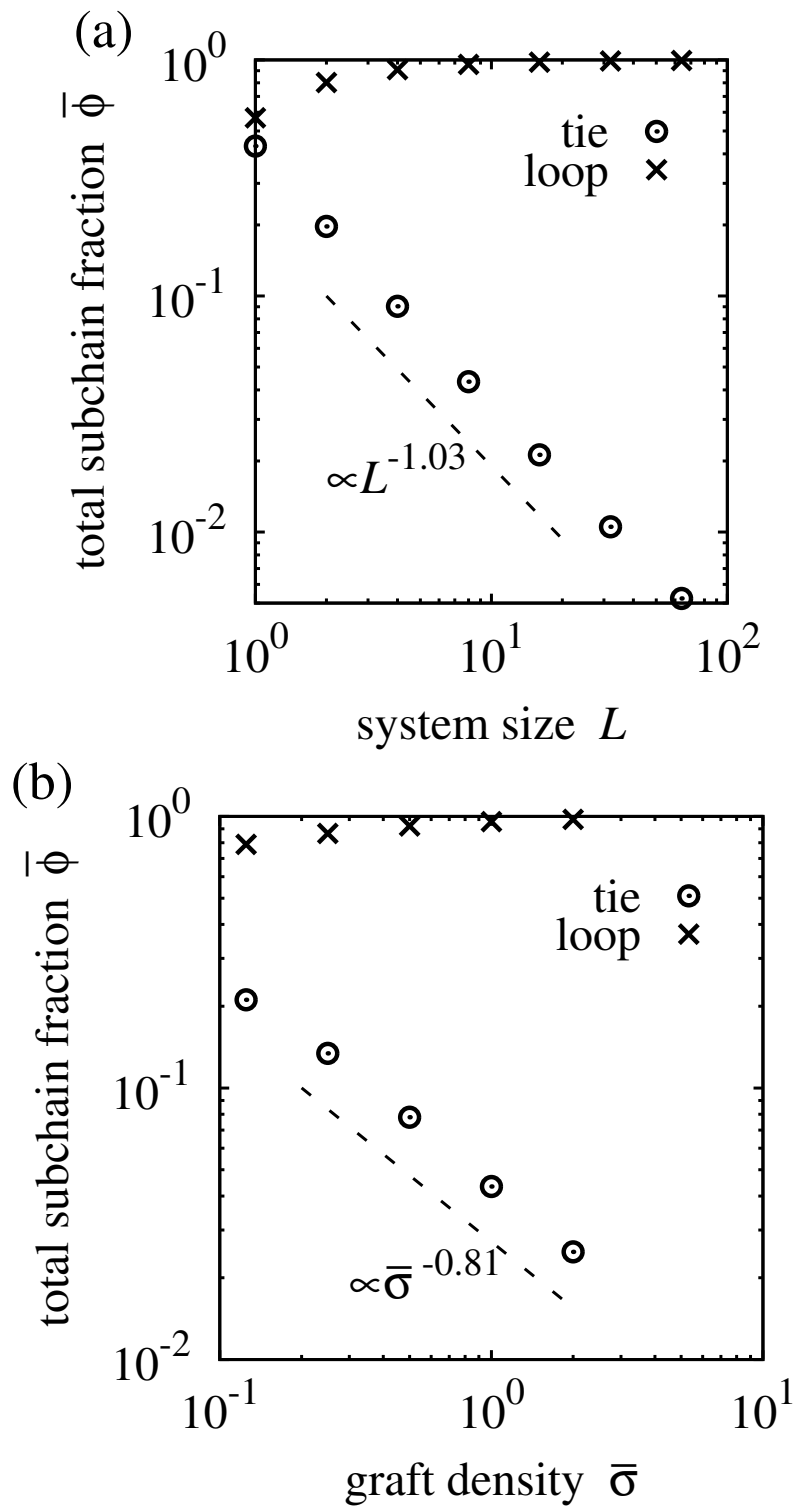


Figure 8:

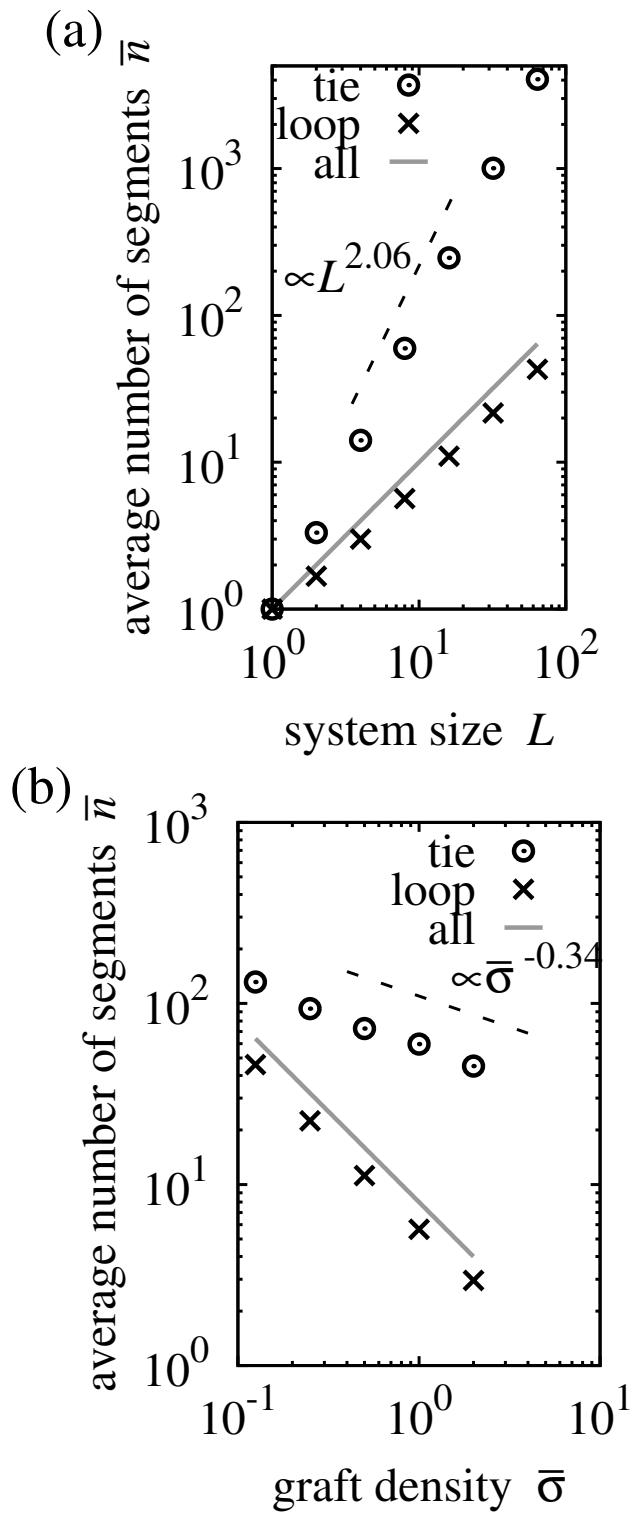


Figure 9:

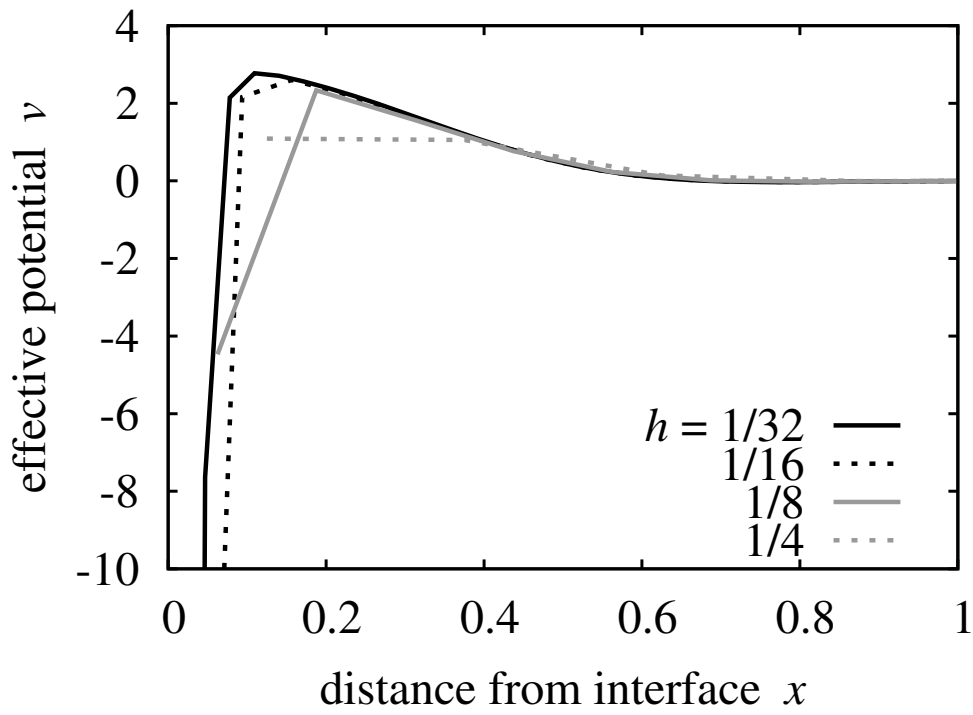


Figure 10:

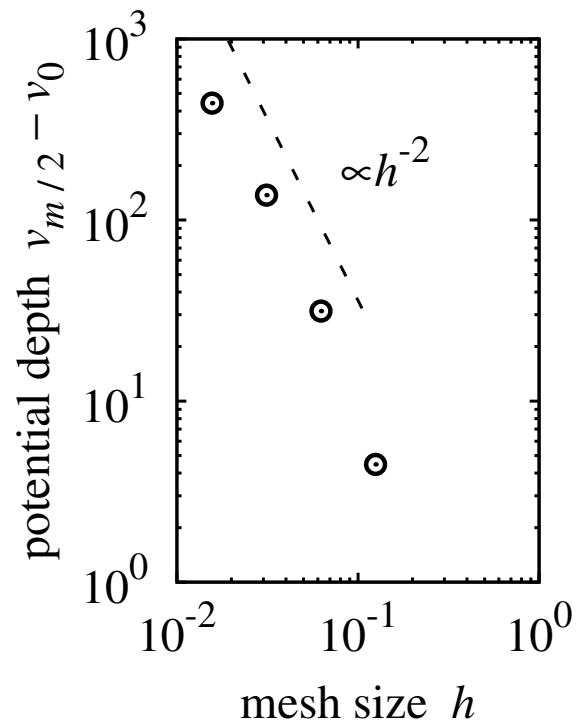


Figure 11:

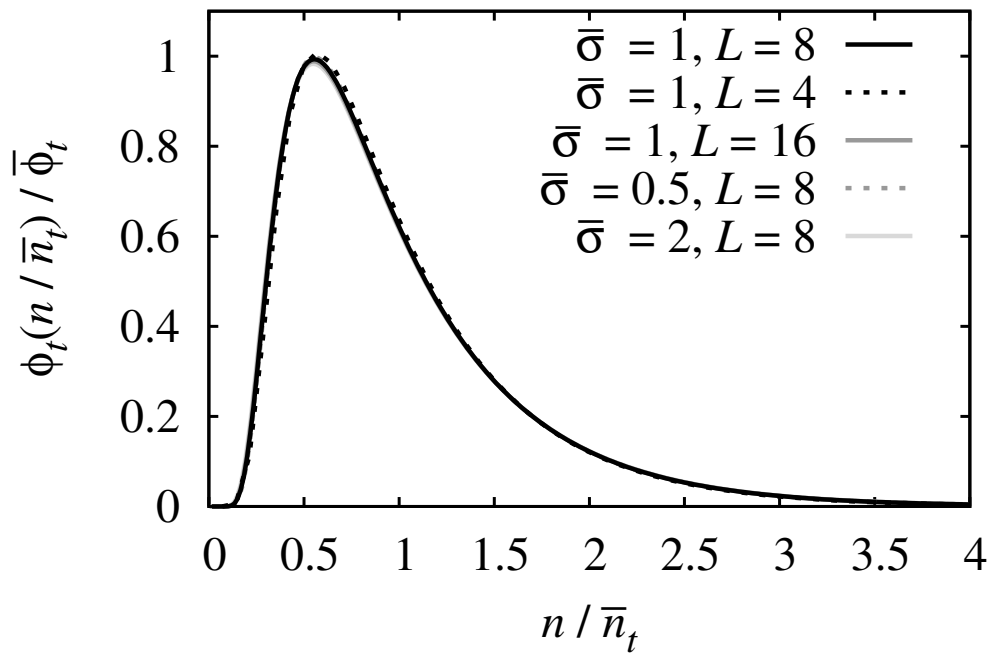


Figure 12:

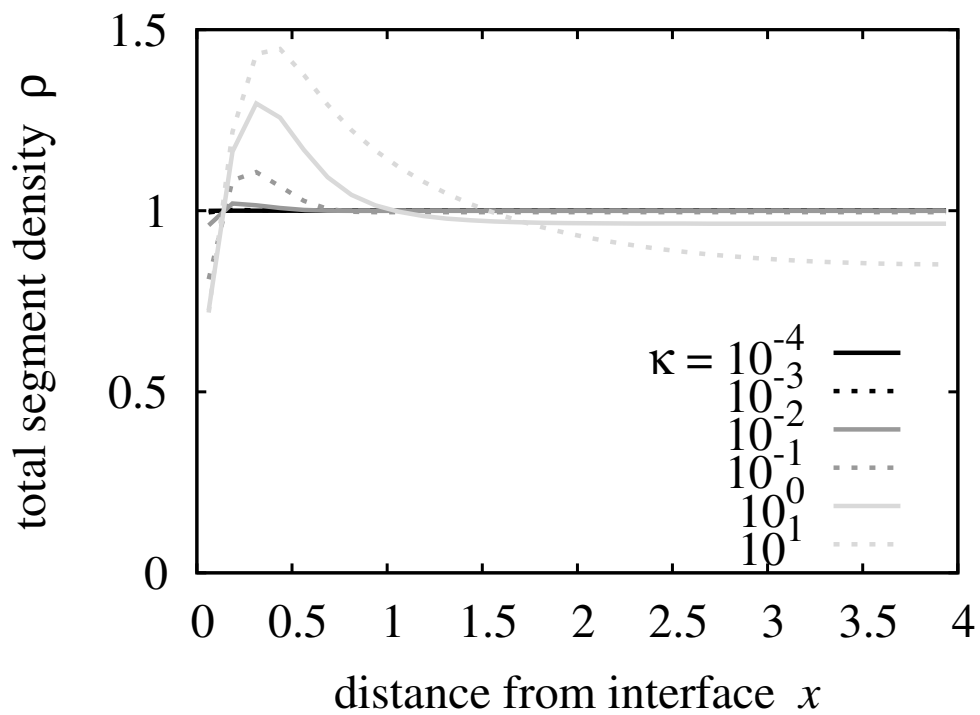


Figure 13:

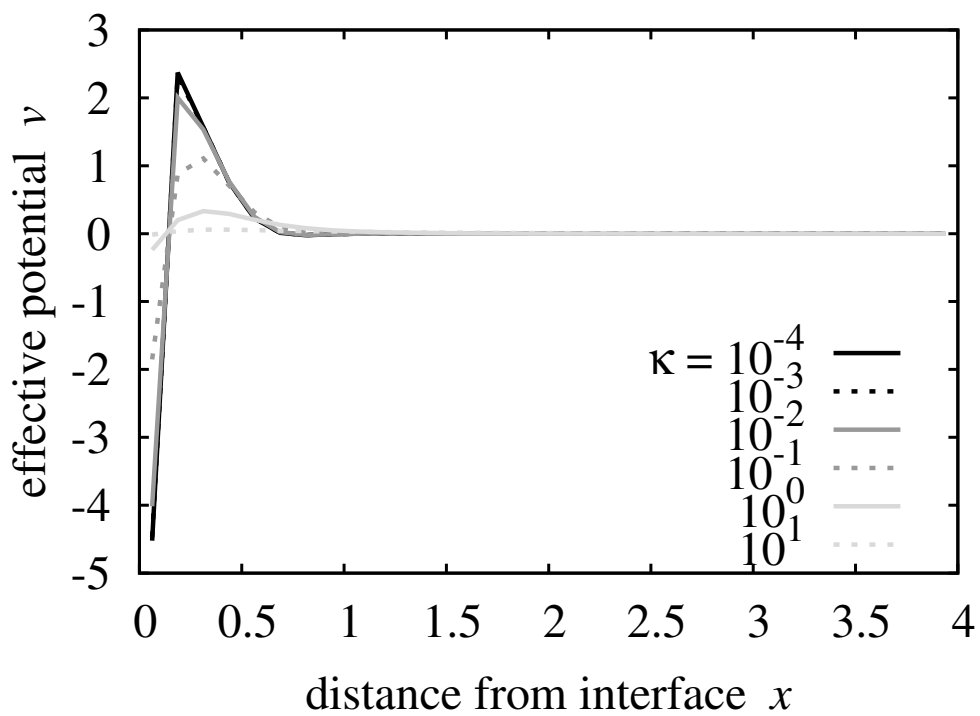


Figure 14: